

pubs.acs.org/JPCB Article

Effects of Nanoparticle Wettability on the Meniscus Stability of Oil-Water Systems: A Coarse-Grained Modeling Approach

Thao X. D. Nguyen, Sepideh Razavi,* and Dimitrios V. Papavassiliou*



Cite This: J. Phys. Chem. B 2024, 128, 3016-3026



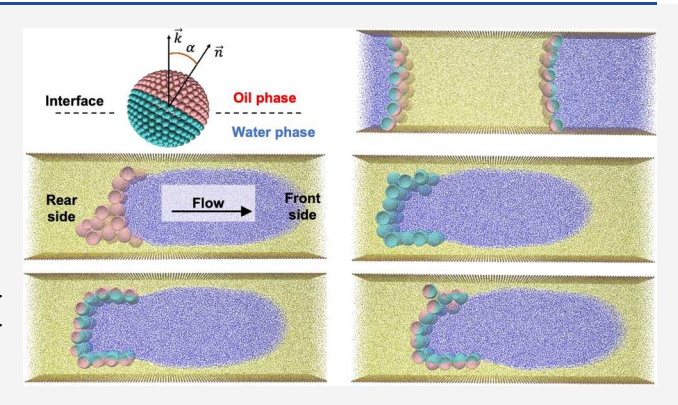
ACCESS

III Metrics & More

Article Recommendations

s Supporting Information

ABSTRACT: A coarse-grained modeling approach is employed to probe the effect of nanoparticles and their wettability on the stability of the interface between two immiscible fluids. In this study, pure oil (dodecane) and water are placed side by side in a nanochannel, forming a meniscus. Homogeneous hydrophilic nanoparticles, Janus particles, and homogeneous hydrophobic nanoparticles are placed at the oil—water interface, and their dynamics are studied as they rearrange at the oil—water interface. The results show that when the water is set in motion, two instabilities occur: the formation of fingers and the detachment of water from the channel wall. It is observed that the formation of fingers is affected by the wettability of the nanoparticles. The second instability may lead to the formation of a drop that



propagates through the channel. However, it is found that the wetting properties of the nanoparticles do not affect the critical flow rate for the detachment of the water from the wall. Therefore, detachment occurs at the same three-phase contact angle regardless of the nanoparticle wetting properties. These findings can be important for industrial applications such as enhanced oil recovery, separation technologies, and microfluidic and nanofluidic technologies.

1. INTRODUCTION

In recent years, the applications of nanotechnology have grown in several areas, such as environmental remediation, 1-3 pharmaceuticals, 4,5 and food processing. 6 In the petroleum exploration and production industry, nanoparticles (NPs) have gained a significant presence in enhanced oil recovery (EOR) since they can affect the characteristics of both the rock where oil is found and the residual oil.⁷⁻⁹ The utilization of NPs in EOR techniques has several advantages, such as adjusting the rheological characteristics of the involved fluids, flexibility in selecting the size and shape of NPs, and chemical modification of the NP surface in order to tune fluid and interfacial properties.¹⁰ Several laboratory studies on NP-enabled EOR have taken place in the past decade. One area of study revolves around investigating the application of hydrophilic silica nanoparticles. Ju et al. 11 indicated that injecting NPs resulted in their adsorption onto pore surfaces, changing the surface wettability and significantly improving oil recovery.

In addition to their impact on surface wettability, NPs can influence the rheological properties of fluid—fluid interfaces depending on their size, shape, surface roughness, and anisotropy, 12–20 which can be employed in tuning the stability of emulsions and foams. 21,22 Among different types of NPs, Janus particles (JPs) stand out, as they combine surface anisotropy and amphiphilicity into a single particle. Because one face of the JPs is hydrophilic and the other is hydrophobic, they exhibit special properties at fluid interfaces. For instance,

the desorption energy from the interface is up to 3 times higher than for homogeneous nanoparticles. ²³ Since the surface anisotropy of JPs can be controlled, the resulting interfacial properties of the particle network can be tuned. Razavi et al. ¹⁴ showed that the amphiphilicity of JPs controlled their collapse behavior at the air—water interface under applied compressive stress, a behavior which was attributed to the orientation of particles and interparticle capillary interactions as the JP amphiphilicity was modified. ²⁰ In addition to experimental investigations, simulations may offer an opportunity to carry out numerical experiments, allowing systematic changes in NP properties and leading to significant contributions to the study of NP characteristics.

Immiscible fluid displacement is widely used in industrial applications, ^{24–26} especially in the oil and gas industry, where chemicals and water are used in EOR. ^{27,28} The method involves injecting a fluid, such as water or gas, into an oil reservoir to displace the oil and push it toward the production wells. The displaced oil is then recovered, which increases the

Received: December 11, 2023 Revised: February 22, 2024 Accepted: February 26, 2024 Published: March 19, 2024





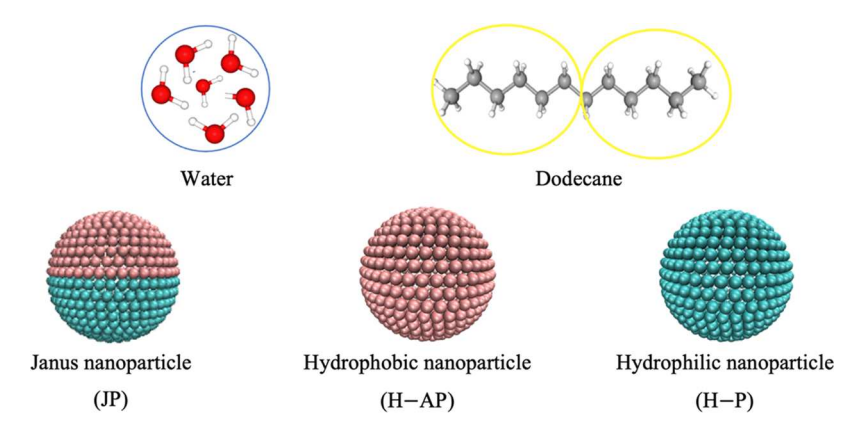


Figure 1. Schematic representation of the beads generated by simulations of DPD with water, dodecane, Janus particles, and homogeneous particles (hydrophilic and hydrophobic nanoparticles). Red, white, and gray spheres represent oxygen, hydrogen, and carbon, respectively. Cyan represents the hydrophilic part, while pink is used for the hydrophobic face of the nanoparticles.

overall production rate. There is a tendency for water to move more readily than oil, leading to instabilities and the development of water fingers. The phenomenon is known as viscous fingering or Saffman-Taylor instability. 29,30 The Saffman-Taylor instability occurs when a fluid pushes a more viscous fluid in a confined space. This is commonly encountered in situations involving porous media or within the gap between two parallel plates (i.e., Hele-Shaw cell³¹). It is essential to predict fingering when dealing with immiscible fluid displacement because it can affect the efficiency of any oil displacement process. However, most studies regarding this instability have been done for two immiscible liquids, whereas in reality, a system consists of many components, such as oil, water, additives, and surface-active species. The establishment of viscous fingering depends on a number of factors, such as the viscosity ratio of wetting and nonwetting fluids, the capillary forces, and the injection rate.³² Several technologies have been developed to avoid fingering, including the modification of the rock wettability by injecting low-salinity water after high-salinity water; 33 varying the pressure gradient or the flow rate of the displacing fluid;³⁴ changing the wettability of the injection fluid by conducting core flood experiments on water-wet and oil-wet cores;³⁵ and using surfactants to modify the interfacial tension.³⁶ Moreover, when viscous fingering occurs, it can create a poor sweep efficiency. Thus, polymers are employed as a viscosity control agent but often degrade in a reservoir with harsh conditions.^{37,38} NPs have been proposed to enhance the viscosity of the polymers in injection fluid by strengthening the thermal stability of the polymer solution and reducing degradation. Numerical simulations by the Lattice Boltzmann method have also been used to investigate viscous fingering, breakthrough times, as well as gravity considerations.

However, a fundamental understanding of the impacts NPs have on the viscous fingering phenomenon still needs to be improved. In particular, the effects of NP wettability on immiscible fluid displacement and the resulting fingering behavior have not been investigated in detail. In this study, we used computations to simulate the flow of water that displaced oil (dodecane) in a nanochannel by using the dissipative particle dynamics (DPD) coarse-graining computational method. The contributions of this paper are to (a) probe how homogeneous particles (hydrophobic or hydrophilic) influence the meniscus at the oil-water interface under equilibrium and nonequilibrium conditions and compare

their behavior to the case when amphiphilic JPs are employed and (b) examine viscous fingering in the presence of NPs at the interface, where the low-viscosity fluid (water) displaces the high-viscosity fluid (oil).

2. METHODS

2.1. Dissipative Particle Dynamics. Instead of individual atoms, DPD models represent clusters of molecules. 40 By Newton's equation of motion, it is possible to calculate the position and velocity of each DPD particle, which is typically called a bead. The model equations are as follows:

$$\frac{\mathrm{d}\mathbf{r}_i}{\mathrm{d}t} = \mathbf{v}_i \tag{1}$$

$$m_i \frac{\mathrm{d}\mathbf{v}_i}{\mathrm{d}t} = \mathbf{f}_i = \sum_{j \neq i} \left(\mathbf{F}_{ij}^{\mathrm{C}} + \mathbf{F}_{ij}^{\mathrm{D}} + \mathbf{F}_{ij}^{\mathrm{R}} \right)$$
(2)

where \mathbf{r}_i and \mathbf{v}_i are the position and velocity vectors of bead i, respectively; m_i is the mass of bead i; and f_i is the force acting on bead i. The total force exerted between two DPD particles i and j includes three components: the conservative (F_{ii}^C) , dissipative (F_{ii}^{D}) , and random (F_{ii}^{R}) forces.⁴¹ The conservative force F_{ii}^{C} is a soft repulsion acting along the line connecting the bead centers and can be calculated as follows

$$\mathbf{F}_{ij}^{C} = \begin{cases} a_{ij} \left(1 - \frac{r_{ij}}{r_{c}} \right) \hat{\mathbf{r}}_{ij} & \text{for } r_{ij} < r_{c} \\ 0 & \text{for } r_{ij} \ge r_{c} \end{cases}$$
(3)

where a_{ii} is a maximum repulsion between beads i and j that controls the type of fluid interactions, $r_{ii} = |\mathbf{r}_i - \mathbf{r}_i|$, $\hat{\mathbf{r}}_{ii} = (\mathbf{r}_i - \mathbf{r}_i)$ $(\mathbf{r}_i)/r_{ij}$, $(\mathbf{v}_{ij} = \mathbf{v}_i - \mathbf{v}_j)$ and (\mathbf{r}_c) is the cutoff radius indicating the distance over which a bead can affect its neighbors. The dissipative or drag force, F_{ij}^{D} , on beads i and j, is given by

$$\mathbf{F}_{ij}^{\mathrm{D}} = -\gamma w^{\mathrm{D}}(r_{ij})(\hat{\mathbf{r}}_{ij} \cdot \mathbf{v}_{ij})\hat{\mathbf{r}}_{ij}$$
(4)

where γ controls friction (along with fluid viscosity), w^D is an rdependent weight function

$$w^{D}(r_{ij}) = \begin{cases} (1 - r_{ij})^{2}, & \text{for } r_{ij} < r_{c} \\ 0, & \text{for } r_{ij} \ge r_{c} \end{cases}$$
 (5)

The random force, F_{ii}^{R} , can be determined by

Table 1. Scaling Factors for DPD Computations

bead density (beads/volume)	number of water molecules in one bead	mass scale (10 ⁻²⁵ kg)	length scale (10 ⁻¹⁰ m)	temperature scale (K)	time scale (10^{-12} s)
5	6	1.80	9.66	298	6.38

$$\mathbf{F}_{ij}^{\mathrm{R}} = \sigma w^{\mathrm{R}}(r_{ij})\theta_{ij}\hat{\mathbf{r}}_{ij} \tag{6}$$

where w^{R} is also an r-dependent weight function, σ controls the amplitude of random motion, ⁴² and the term θ_{ij} is a Gaussian white noise function that is calculated as

$$\langle \theta_{ij}(t) \rangle = 0, \ \langle \theta_{ij}(t)\theta_{kl}(t') \rangle = (\delta_{ik}\delta_{jl} + \delta_{il}\delta_{jk})\delta(t - t')$$
 (7)

where t is time, δ_{ij} is the Kronecker delta, and $\delta(t-t')$ is the Dirac delta function. ⁴³

As Espanol and Warren demonstrated,⁴³ the weight functions w^D and w^R are related to each other as follows:

$$w^{D}(r) = [w^{R}(r)]^{2}$$
 (8)

and

$$\sigma^2 = 2\gamma k_{\rm B} T \tag{9}$$

where T is the system temperature and k_B is the Boltzmann constant.

2.2. Simulation Details. To perform all calculations, the software package Large-scale Atomic/Molecular Massively Parallel Simulator (LAMMPS) was used. Figure 1 shows a schematic configuration of all species used in the DPD simulations, and Table 1 shows the time and length scales for converting DPD units to physical units.

Figure 1 shows that each water bead (W) consisted of six water molecules and each dodecane molecule (C₁₂H₂₆) contained two oil beads (O). The dimensions of the nanochannel were 90 \times 10 \times 31 r_c^3 (using dimensionless DPD units in the x, y, and z directions), with the fluid density set as 5 in DPD units (i.e., 5 DPD beads per unit volume of the simulation).⁴¹ Therefore, 138,600 fluid beads in the computational domain and 2938 wall beads were added to the system. The distance between neighboring NP beads was set at 0.30 r_c , and the diameter of the particles was set to 4.7 r_c (~3.64 nm). 45 By adjustment of the interaction coefficient a_{ij} in eq 3, different types of NPs can be generated, including hydrophilic or hydrophobic nanoparticles and JPs with hydrophilic and hydrophobic phases. The NPs were placed on the oil-water interface. The interaction parameters used in this study are listed in Tables 2 and 3. The selection of the interaction

Table 2. Values of the Repulsion Parameter (a_{ij}) Used in the Simulations^a

	O	W	Phi	Pho	wall
0	15	129	a ^b	c ^b	20
W		15	b^{b}	d^{b}	30
Phi			15	25	35
Pho				15	15.5
wall					15

"W and O represent water and oil, respectively, while the NPs include hydrophilic (Phi) and hydrophobic (Pho) beads. "The values of a, b, c, and d that represent the interaction parameters of hydrophilic—oil (Phi—O), hydrophilic—water (Phi—W), hydrophobic—oil (Pho—O), and hydrophobic—water (Pho—W) beads, respectively, are provided in Table 3.

Table 3. Values of the Repulsion Parameters (a_{ij}) for Different Types of Nanoparticles

type of nanoparticle		Phi-O	Phi-W	Pho-O	Pho-W
A (hydrophobic nanoparticle)				15	50
Janus nanoparticle	B (3528-2530)	35	28	25	30
	C (3530-2540)	35	30	25	40
	D (5530-2540)	55	30	15	40
	E (5530-2580)	55	30	25	80
	F (2520-1550)	25	20	15	50
G (hydrophilic nanoparticle)		25	20		

parameter between dodecane and water was based on the interfacial tension between these two fluids (Supporting Information). In the case of JPs, our study simulates a particular JP type where one facet corresponds to an amidine polystyrene latex (APSL) surface, while the opposing facet represents the wettability of gold surface. The interaction parameters with the oil and the water have been determined by matching the available experimental data on the three-phase contact angle of particles at the oil-water interface. 45 This case was marked as the nanoparticle F; for the rest of the JP cases, the interaction parameter between each face of the Janus particle and the fluid phases were altered in order to simulate JPs with different degrees of amphiphilicity. 46 The hydrophobic NPs (type A) and hydrophilic NPs (type G) used in our simulation represent APSL and gold, respectively, exhibiting surface characteristics corresponding to JP type F.

The configuration of JPs and their corresponding alignment at the interface was investigated by measuring the angle between the orientation alignment vector and the interface. The polar angle (α) is defined as the angle between the normal vector \vec{k} that is perpendicular to the oil—water interface and the vector \vec{n} connecting the particle center and a selected bead (top or bottom) on the surface of the particle (see Figure 2). This angle could take values from 0 (i.e., a Janus NP with its cap up) to 180° (i.e., Janus cap down).

The difference in wettability between the two surfaces determines the degree of amphiphilicity of a JP. It is defined as $\Delta\theta = \frac{\theta_{\rm Phi} - \theta_{\rm Pho}}{2}$, where $\theta_{\rm Phi}$ and $\theta_{\rm Pho}$ describe the contact angle between an oil droplet and a flat surface with the same wettability as the hydrophilic and the hydrophobic faces of the Janus particle, respectively, as seen in Figure 2b,c. 14 As was shown in previous research, 47 the three-phase contact angle of the oil droplet on a flat surface; i.e., θ_{Phi} or θ_{Pho} , can be determined from the density profile of the droplet. The amphiphilicity of the Janus particle can be tuned by modifying the wetting behavior of the two opposing JP facets. In our simulations, this adjustment was achieved by enhancing the affinity of each JP facet for the water phase, resulting in the modification of $\Delta\theta$, which, in turn, impacted the polar angle α , seen in Figure 2a. For example, a homogeneous particle (zero amphiphilicity) has $\Delta\theta = 0^{\circ}$, while an anisotropic JP with

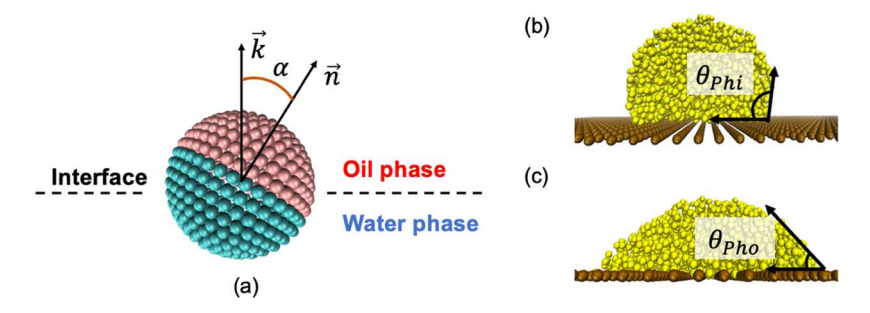


Figure 2. (a) Schematic illustrating the polar angle (α) between vector \vec{n} perpendicular to the Janus cap and vector \vec{k} normal to the oil—water interface. Cyan is used to signify the hydrophilic face of the Janus particle, whereas pink is used to indicate the hydrophobic surface. The three-phase contact angle formed by the oil droplet on a solid flat surface that exhibits the same wetting behavior as the hydrophilic facet of the JP is referred to as θ_{Phi} and is shown in (b). The three-phase contact angle formed by the oil droplet on a solid flat surface that exhibits the same wetting behavior as the hydrophobic facet of the JP is referred to as θ_{Pho} and is shown in (c). Yellow spheres indicate the oil beads, whereas the water beads are removed for the sake of clarity.

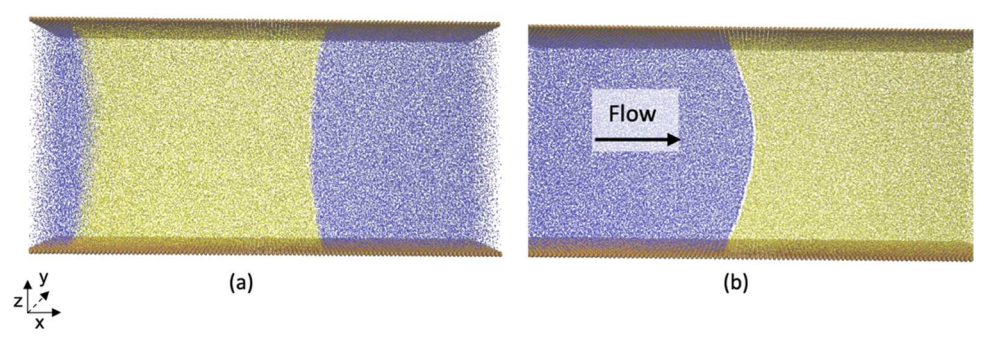


Figure 3. Two snapshots of the DPD model depict the oil and water meniscus located between two solid walls under (a) no flow and (b) a Poiseuille flow. Ocher, blue, and yellow colors were applied to represent the wall, water, and oil beads, respectively.

strong amphiphilicity is expected to align its equator with the interface, and result in a polar angle $\alpha = 0^{\circ}$.

To set up the computations in the nanochannel, first, a viscous fluid (oil) was placed in the channel, surrounded by a lower-viscosity fluid (water), so a meniscus was formed across the nanochannel (Figure 3a). After equilibrium was reached, a body force was applied to the lower-viscosity fluid so that it might displace the higher-viscosity fluid in the channel (see Figure 3b). In this study, a Poiseuille flow was used, driven by a pressure gradient applied in the DPD simulation as a body force in the x direction. No-slip boundary conditions had to be applied at the inner solid surface of the channel based on the methodology reported previously:⁴⁸ (1) freeze each wall bead in order to avoid the migration of liquid beads into the wall beads, (2) apply the bounce-back boundary condition at a distance from the inner walls equal to 0.1 DPD units, and (3) increase the friction coefficient between solid and liquid beads by 2-fold relative to the value used for fluid—fluid interactions. Periodic boundaries were applied in the other two directions.

The system was initially run with the NVE ensemble (i.e., constant number of particles, volume, and energy) to attain thermal equilibrium before further analysis. This was applied for 10,000 time steps. Recognizing the possibility of temperature fluctuations under nonequilibrium conditions, we employed a direct temperature rescaling thermostat for the subsequent time steps by rescaling the velocities of the particle every 200 time steps. This rescaling affected only translational degrees of freedom. As a result, the temperature remained constant at T=1, employing the DPD units of temperature. The simulation time step was set to $\Delta t=0.02$ in DPD units. The total number of time steps was 1,000,000. The software

program applied for visualizing system snapshots is the visual molecular dynamics (VMD).⁴⁹

3. RESULTS AND DISCUSSION

3.1. Characteristics of Nanoparticles and Their Behavior at the Oil-Water Interface. In order to verify that the computations accounted for the physical behavior of the system, the NP behavior at the oil-water interface was investigated first. The rotation of JPs when placed at a flat interface under different initial conditions is shown in Figure 4. The NPs were initially placed at the oil-water interface with various orientations denoted by the angle α , including $\alpha = 0^{\circ}$ (Figure 4a); $0^{\circ} < \alpha < 180^{\circ}$ (Figure 4d), and $\alpha = 180^{\circ}$ (Figure 4g). Over the simulation time, a single NP commenced rotating (Figure 4b,e,h) until it rested in its preferred position at equilibrium (Figure 4c,f,i). It is thus confirmed that the hydrophilic side of the JP tends to be in contact with the water phase, whereas the hydrophobic face exhibits an affinity for the oil phase regardless of the initial orientation of a particle at the interface.

Measurements of the three-phase contact angle of oil droplets in the water phase were carried out to evaluate the wettability of hydrophilic and hydrophobic surfaces of NPs on solid surfaces mimicking the JP faces. Using the example of the JP (Case F), it was determined that the average droplet contact angle on the surface of a solid wall was $\theta_{\rm Phi}\approx 95.6\pm 2.6^{\circ}$ on the hydrophilic side, whereas oil was spreading on the hydrophobic surface corresponding to $\theta_{\rm Pho}\approx 0^{\circ}$. The degree of amphiphilicity can be estimated as $\Delta\theta=\frac{\theta_{\rm Phi}-\theta_{\rm Pho}}{2}\approx 47.8^{\circ}$. The results for each Janus particle are summarized in Table 4.

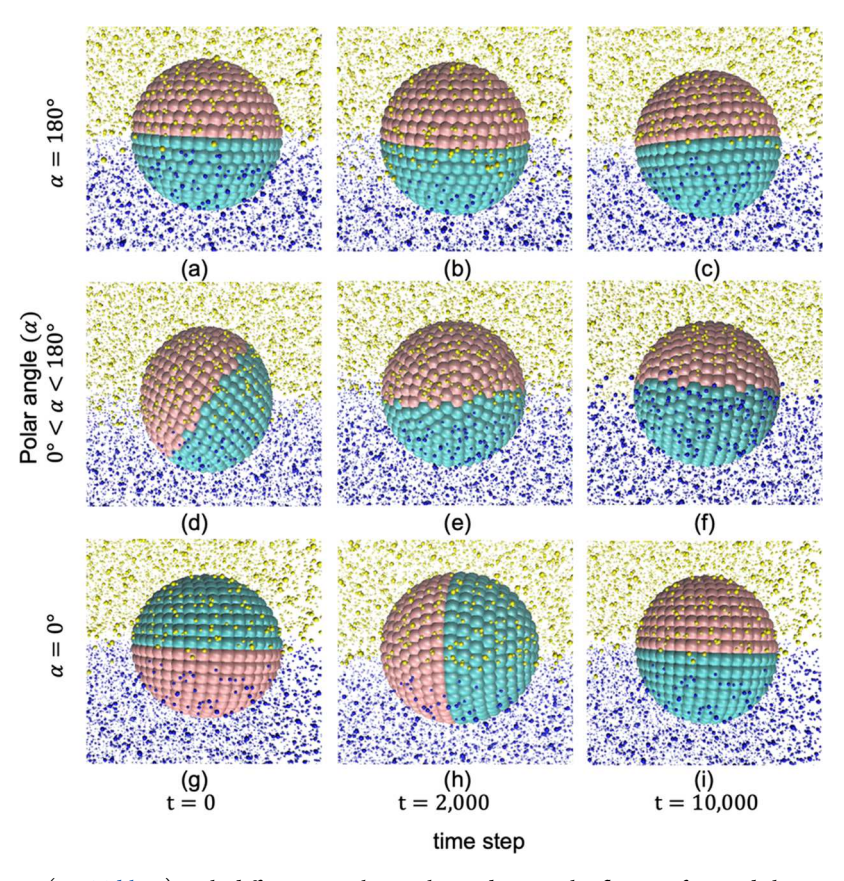


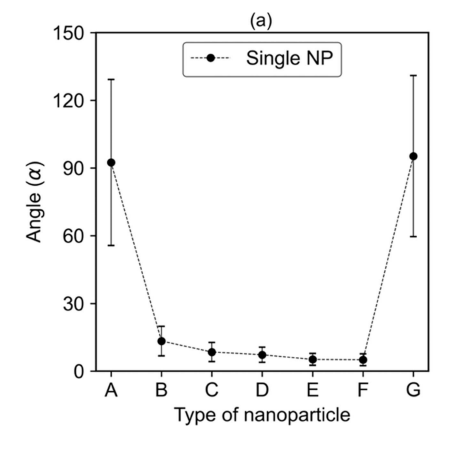
Figure 4. Janus particle type F (see Table 4) with different initial α -angle residing on the flat interface and the progression of its configuration during the DPD simulation. (a–c) The scenario where α = 180° for time steps 0, 2000, and 10,000, respectively; (d–f) the case where 0° < α < 1 80° for time steps 0, 2000, and 10,000, respectively; (g–i) the case of α = 0° for time steps 0, 2000, and 10,000, respectively. The water and oil beads are exhibited as blue and yellow, respectively. Cyan represents the hydrophilic part of the nanoparticle, while pink is used for the hydrophobic face.

Table 4. Amphiphilicity of Different Types of Nanoparticles

type of nar	$\Delta heta$	
A (hydrophobic nanopa	A (hydrophobic nanoparticle)	
Janus nanoparticle	B (3528-2530)	$10.7 \pm 1.0^{\circ}$
	C (3530-2540)	$13.9 \pm 1.5^{\circ}$
	D (5530-2540)	$17.3 \pm 1.5^{\circ}$
	E (5530-2580)	$31.0 \pm 1.0^{\circ}$
	F (2520-1550)	$47.8 \pm 1.3^{\circ}$
G (hydrophilic nanopar	ticle)	0°

Altering the interaction parameter between the faces of the Janus particle and the fluid phases results in a change in JP amphiphilicity. Two types of homogeneous nanoparticles (i.e., no amphiphilicity) were considered, in addition to five types of JPs in which the degree of amphiphilicity was altered.

The change in the orientation of JPs at the interface with their amphiphilicity can be examined by placing the particles at a flat oil—water interface to study the effect independent of the curvature of the meniscus. The meniscus curvature might be affected by the width of the nanochannel and/or the wetting



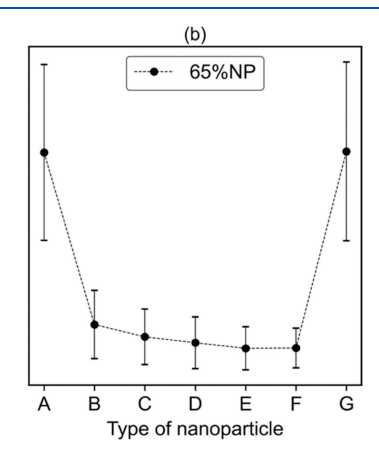


Figure 5. Impact of particle amphiphilicity on its orientation alignment at the interface for (a) a single nanoparticle and (b) 65% nanoparticle coverage. The error bars represent two standard deviations obtained in each case.

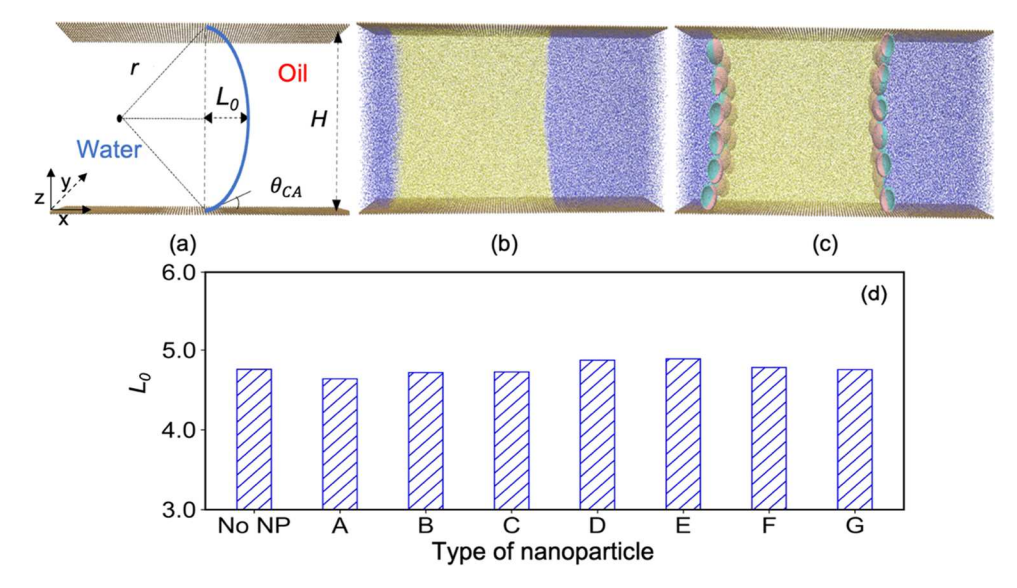


Figure 6. (a) Schematic illustration of the simulation geometry for an oil—water meniscus confined between two solid walls. Equilibration of an oil droplet on a solid wall at different stages of the DPD computation for a system with (b) oil and water and (c) oil, water, and nanoparticles at equilibrium. The ocher, blue, and yellow colors represent the wall, water, and oil beads, respectively. Cyan is displayed to indicate the hydrophilic part of the nanoparticle, while pink represents the hydrophobic face. (d) Comparison of the finger length between different cases.

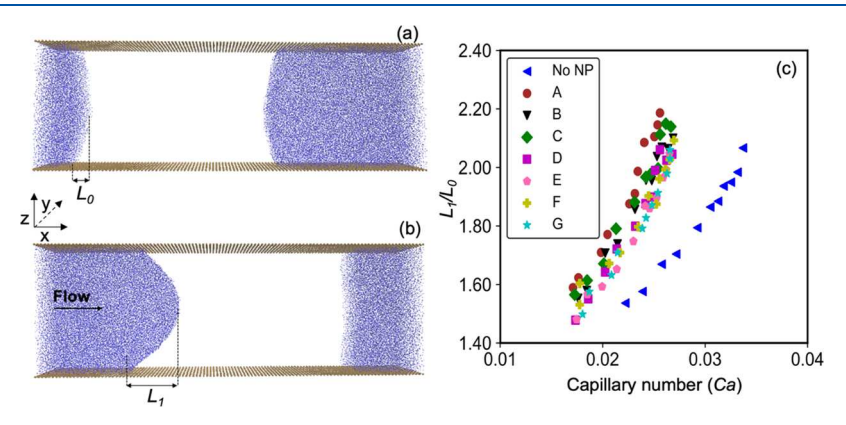


Figure 7. Illustration of the finger pattern (a) L_0 at 10,000th time step in the absence of flow and (b) L_1 at 34,000th time step in the presence of a Poiseuille flow with a body force of $g_x = 0.0057$. The wall and water beads are depicted using other and blue, respectively. (c) Ratio of finger lengths $\left(\frac{L_1}{L_2}\right)$ as a function of the capillary number (Ca) with different nanoparticle amphiphilicity.

behavior of the channel walls. It is clearly shown in Figure 5 that the particle configuration at the flat interface depends on the difference in amphiphilicity when no flow is present. The homogeneous particles rotated freely at the interface with large fluctuations in the orientation angle (α) ; in contrast, the rotational freedom of JPs is limited (Figure 5a). These results agree with previous findings that JPs of high amphiphilicity are expected to have limited orientational freedom.¹⁴ There is a slight decrease in the angle α as the amphiphilicity of the JPs is enhanced, while there is no preferred orientation angle as the homogeneous particles freely rotate at the interface, as displayed in Figure 5b. Moreover, this trend is observed regardless of the number of particles present at the interface. A minor variation in orientation degree is shown for the case of NPs that cover 65% of the interface area and when only one NP is present at the interface. This is likely a result of the interaction between NPs. The percentage of NP coverage at the oil-water interface (c_{NP}) was determined as follows: $c_{\rm NP} = n \times \frac{\pi \times R_{\rm NP}^2}{S}$, where *n* is the total number of NPs, $R_{\rm NP}$ is

the radius of NP, and *S* is the total interfacial area between the oil and water phases.

Next, the impact of NPs on the stability of the oil—water interface and the role of amphiphilicity was examined. 65% of the interfacial area was covered by the NPs at the oil—water interface. The initial finger length at equilibrium, L_0 , is the maximum distance between the apex of the meniscus and the 3-phase point of contact at the nanochannel wall in the x-direction (see Figure 6). The contact angle $\theta_{\rm CA}$ is the three-phase contact angle between the oil phase and the solid wall (Figure 6a). If the contact angle $\theta_{\rm CA}$ is altered, then the length of the finger will change. Assuming that the meniscus is the arc of a circle, the three-phase contact angle and the L_0 are related as follows:

$$\theta_{CA} = \frac{\pi}{2} - \arctan\left(\frac{\frac{H}{2}}{r - L_0}\right) \tag{10}$$

where H is the height of the channel and r is the radius of the water droplet forming the meniscus, $r = \frac{\frac{H}{2}}{\sin(\frac{\pi}{r} + \theta_{r_A})}$.

Figure 6b,c depicts a snapshot of the oil—water system without and with NPs in a channel, respectively. The change of the length of the meniscus at equilibrium, L_0 , as a function of particles amphiphilicity is plotted in Figure 6d. There were no significant changes observed due to the fact that the oil—water interfacial tension (IFT) does not change (see Figure S1), in accordance with the findings of previous studies. This indicates that the length of the meniscus is not influenced by the presence of NPs at equilibrium.

3.2. Meniscus Stability under Flow. 3.2.1. Fingering. Water is a low-viscosity fluid compared to oil. When water displaces a higher-viscosity fluid, fingering may be observed depending on the flow conditions. In the simulations, the velocity of the water phase was increased up to the point at which droplets appeared to allow for the determination of finger length. The development of fingering instabilities at the meniscus can be characterized by dimensionless numbers, typically the capillary number (Ca), expressed as $Ca = \frac{\mu \times V}{\text{IFT}}$, where μ is the dynamic viscosity of the displacing fluid (water), V is the velocity of water, and IFT is the interfacial tension between the oil and water phases. Although the IFT did not change when NPs were added at the oil-water interface, Ca was affected by viscosity, velocity, and the different wetting properties of NPs. In this study, the maximum velocity of water was increased by changing the external body force, which created the Poiseulle flow, resulting in the rise of the Ca

As shown in Figure 7a, the equilibrium finger length (L_0) is determined by a computation without flow, whereas Figure 7b illustrates the dynamic finger length (L_1) calculated in the presence of flow. The instability of the meniscus is influenced by the presence of NPs located at the oil—water interface, resulting in a change in $\frac{L_1}{L_0}$ ratio. Figure 7c shows a plot of the dependence of the finger length ratio, $\frac{L_1}{L_0}$, on the capillary number. As expected, an increase in Ca leads to a corresponding increase in the length of the finger. A straight line can be fitted to the simulation data for different cases, providing an equation of the following form:

$$\frac{L_1}{L_0} = m \times Ca + n \tag{11}$$

The slope of the line (m), the y intercept (n), and the coefficient of determination (R^2) for all different cases simulated are listed in Table 5.

Table 5. Coefficients Appearing in Eq 11 and the Coefficient of Determination (R^2)

case	m	n	R^2
hydrophobic NP	68.4	0.4	0.97
all types of JPs	59.8	0.5	0.93
hydrophilic NP	60.1	0.4	0.97
no NPs	44.0	0.5	0.98

In Table 5, it can be seen that when NPs are present in the system, there is a higher slope of the line compared to the case with no NPs. Therefore, the presence of particles at the fluid interface, either JPs or homogeneous NPs, has an impact on the fingering phenomenon. The deformation of the meniscus exhibits variation, depending on the type of nanoparticles. The bigger difference is observed for homogeneous NPs,

particularly in the case of hydrophobic NPs with m=68.4, while for hydrophilic NPs, the slope is m=60, driven by disparities in their surface wetting characteristics. The JP amphiphilicity, however, does not appear to affect the slope of the line, as seen in Figure 7 and Table 5. The effects of NPs on the stability of the oil—water interface are also examined by comparing the Ca at the point of significant fingering, identified as the point at which the finger length L_1 is at least twice the value of L_0 ; i.e., the ratio of $\frac{L_1}{L_0}$ is greater than 2.

As seen in Figure 8, if the NPs are present in the oil—water system, the *Ca* needed to reach the same finger length was smaller when compared to the bare oil—water system. This phenomenon occurs because NPs lead to a change in the shape of the deformed meniscus when adsorbed onto the oil—water interface. Therefore, the oil—water meniscus is more stable in a system without NPs. In other words, a much higher water velocity is required to observe the same ratio of finger lengths when NPs are not present.

3.2.2. Detachment. As the water velocity increases, the second instability occurs. Water detaches from the walls, and a water droplet forms that flows in the center region of the nanochannel. Hydrophobic solid walls were used in this study, causing the oil phase to attach to the walls and leading to water droplet creation at the center of the channel. The values of the three-phase contact angle at which the detachment of the water phase from the solid wall occurs are provided in Figure 9. Despite the different types of NPs, there appears to be a critical three-phase contact angle that is consistent at $\theta_{CA} = 48.9 \pm 2.7^{\circ}$.

After detachment occurs, the form of the water droplet resembles the formation of a Taylor bubble in classical twophase flow cases. This elongated bubble remains slender and occupies nearly the entire cross section of the channel as it moves through it. A Taylor bubble consists of four main components:⁵³ (1) a nose that resembles a hemisphere, (2) a central region encompassed by a developing film, (3) a developed film, and (4) a tail wake (see Figure 10). The value of the body force required to reach the critical contact angle for the detachment of water to create a droplet is shown in Figure 10a. The required critical body force does not display significant differences whether NPs are present or not (it is within 4%, with no systematic trend). The behavior of NPs once a drop is formed was examined in detail to gain a better understanding of how different types of NPs impacted the droplet shape in the channel. In principle, the water droplet tends to move forward, whereas the oil phase around the water droplet moves under the push of water, creating a slip velocity. Besides, as the water droplet moved to the center of the channel under the Poiseuille flow, NPs rearranged at the oilwater interface. It is seen that the NPs migrated to the rear side of the droplets for all cases (Figure 10b-e). Similar observations have been reported for surface-active species (i.e., surfactants) by Luo et al.54 It was shown that the surfactant exhibits a tendency to move across the surface of the droplet, traversing from the front to the rear. Distinct from the surfactants used in the study carried out by Luo et al., the surface-active species in our simulation are NPs, but those findings provide qualitative evidence to support the reliability of our results.

In the computations presented here, the formation of a second water droplet after detachment was not observed. Additional computations (not presented here) with a

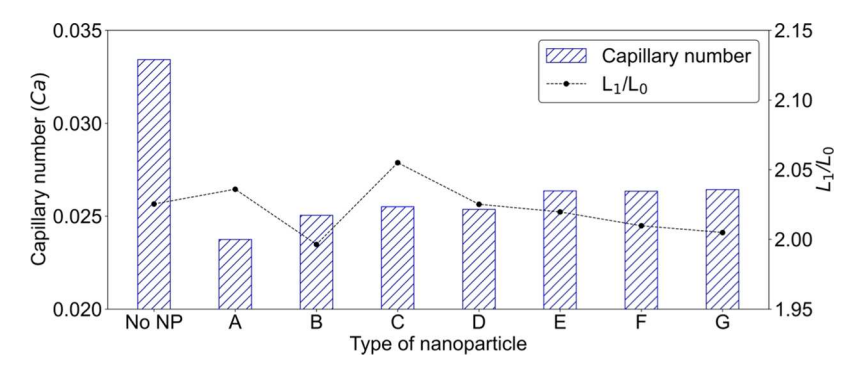


Figure 8. Capillary number at which the finger length ratio is the same $\left(\frac{L_1}{L_0} \approx 2\right)$ as a function of the NP wettability.

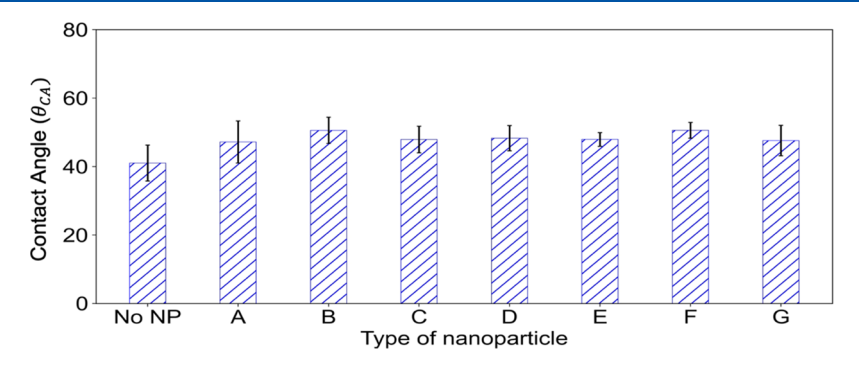


Figure 9. Three-phase contact angle (θ_{CA}) through the oil phase when detachment of the water occurs. The same number of nanoparticles were located at the oil—water interface, corresponding to 65% particle surface coverage. The error bars were calculated by the standard deviation of three contact angle measurements.

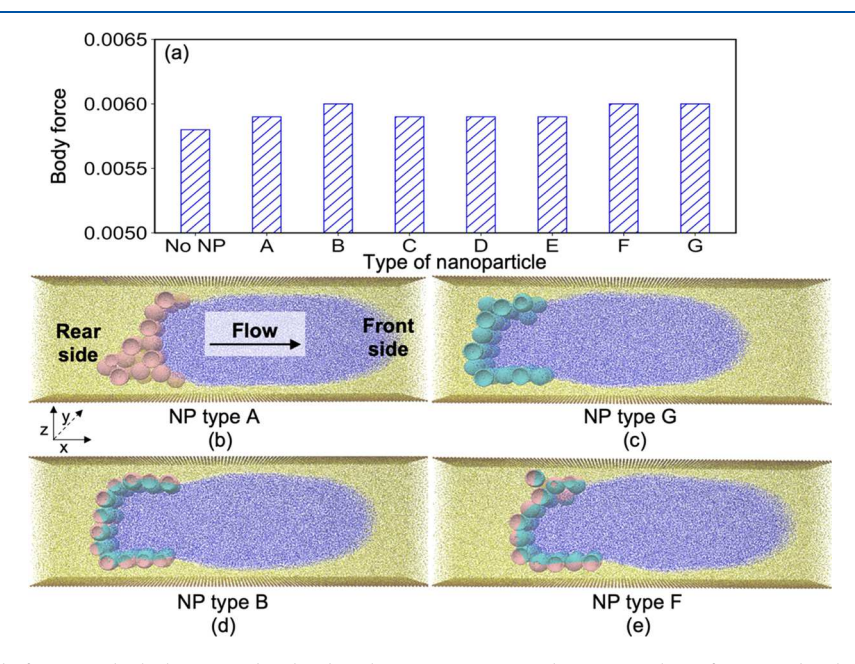


Figure 10. (a) Critical body force at which the water droplet detachment occurs. Simulation snapshot of a water droplet with nanoparticles located at the oil—water interface, including (b) hydrophobic nanoparticles, (c) hydrophilic nanoparticles, and Janus nanoparticles with (d) $\Delta\theta = 10.7^{\circ}$ and (e) $\Delta\theta = 47.8^{\circ}$. The colors used to represent the wall, water, and oil beads are ocher, blue, and yellow, respectively. The color cyan indicates the hydrophilic part of the nanoparticles, and the hydrophobic face is denoted by the color pink.

computational box twice as long or twice as wide did not reveal the formation of a second droplet. While droplet breakup has been observed in different situations with many-body DPD (MDPD), 55,56 the primary focus in the present work is to examine the behavior of a meniscus with the presence of NPs at the oil—water interface and the detachment of water

droplets from the walls. The standard DPD technique serves as a good tool for investigating this issue.

Next, we examined how NPs were arranged when the droplet shape took its final form since the NP arrangement can affect the final shape, size, and behavior of the resulting droplets. As seen in Figure 10b-e, the NPs mostly remained at

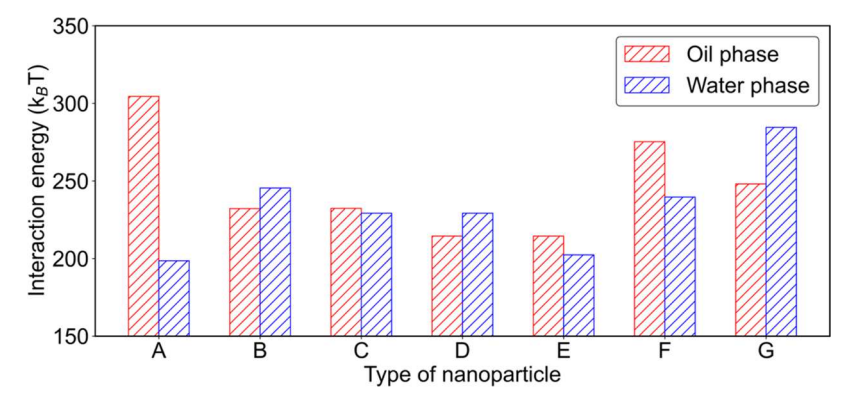


Figure 11. Interaction energy of one nanoparticle with oil or water plotted as a function of the different NP amphiphilicity.

Table 6. Average Interaction Parameters for the Oil Phase and Water Phase Applied for Different Types of Nanoparticles

particle type		$\Delta heta$	$\frac{a_{\text{P-O}} + a_{\text{AP-O}}}{2}$	$\frac{a_{\text{P-W}} + a_{\text{AP-W}}}{2}$	favored phase for partition
A (hydrophobic nanoparticle)		0°	7.5	25	oil
Janus nanoparticle	B (3528-2530)	10.7°	30	29	oil—Water
	C (3530-2540)	13.9°	30	35	oil
	D (5530-2540)	17.3°	40	35	water
	E (5530-2580)	31.0°	40	55	oil
	F (2520-1550)	47.8°	20	35	oil
G (Hydrophilic nanoparti	icle)	0°	12.5	10	water

the oil-water interface. In a few instances, some of the NPs migrated into one of the two fluid phases depending on the particle wetting properties. To determine which phase might be preferred by the NPs when they were forced to partition into one of the fluids, the NP interaction energy between a single NP and either oil or water was calculated in a separate set of computations. The NPs were placed in the simulation box with only one fluid phase (only oil or only water), and the interaction energy was calculated starting from the 10,000th time step and then averaged over the next 1,000,000 time steps. As seen in Figure 11, each type of NP exhibits different interaction energies. This can be explained as follows: A higher interaction energy when an NP is in the oil phase than when it is in the water phase indicates a stronger attraction between NPs and the oil phase. In other words, the NPs are more likely to partition into the oil phase than in the water phase. The cause of this behavior could be attributed to variations in the surface chemistry of the NPs, which are determined by the interaction parameters used in the simulations. Table 6 presents the changes in the average interaction parameters between the hydrophilic or hydrophobic substrate of the NPs and the oil or water phase. The favored phase is also indicated in Table 6, where it is confirmed that the preferred phase is the one in which the average repulsion is the lowest. Particles of type B, where the affinity for either fluid phase is similar, tend to remain at the interface as they modify the shape of the drop (Figure 11d). In other cases, such as particles of type F seen in Figure 11e, a few particles migrate to the oil phase instead of modification of the drop shape.

4. CONCLUSIONS

In summary, we investigated the influence of different types of NPs on the meniscus of oil and water in the channel, including homogeneous nanoparticles (hydrophobic or hydrophilic) as well as amphiphilic Janus nanoparticles with or without flow, using coarse-graining simulation methods. At equilibrium, the

Janus particle's hydrophilic face reoriented to be in contact with the water phase, while its hydrophobic surface exhibited a tendency to face the oil, regardless of the JP's initial orientation at the interface. From the calculated oil—water IFT values for the case of NPs located at the oil—water interface, it can be concluded that NPs do not affect the IFT in any significant way, leading to minimal change in the equilibrium meniscus length, L_0 .

Under an applied Poiseuille flow, a linear relationship appears to apply between the finger length and capillary number. The wettability of the NPs affects meniscus stability, while the presence of hydrophobic particles increases fingerlike protrusions of water in oil. In contrast, detachment of the water droplet occurs only when the three-phase contact angle reaches the critical value of $48.9 \pm 2.7^{\circ}$, which is independent of the type of particles. Furthermore, the fluid velocity is also important. We have found that the pressure difference is more important for detachment from the wall and droplet formation, as low-viscosity fluid displaces another fluid than the properties of the particles, specifically when NPs are introduced into an oil and water mixture. Finally, once a drop is formed, the NPs do not distribute uniformly across the droplet surface, but instead they form more densely packed patches on the rear side of the drop. The NPs rearrange themselves on the oilwater interface, and they might even partition into the oil or water phases at the rear of the drop. The phase to which they might partition depends on their surface chemistry.

ASSOCIATED CONTENT

Supporting Information

The Supporting Information is available free of charge at https://pubs.acs.org/doi/10.1021/acs.jpcb.3c08092.

Dodecane—water interfacial tension determined through independent calculations employing a system with two flat oil—water interfaces in the presence of nanoparticles (PDF)

AUTHOR INFORMATION

Corresponding Authors

Sepideh Razavi — School of Sustainable Chemical, Biological and Materials Engineering, The University of Oklahoma, Norman, Oklahoma 73019, United States; orcid.org/0000-0003-1225-6081; Email: srazavi@ou.edu

Dimitrios V. Papavassiliou — School of Sustainable Chemical, Biological and Materials Engineering, The University of Oklahoma, Norman, Oklahoma 73019, United States; orcid.org/0000-0002-4583-0820; Phone: (405) 325-5811; Email: dvpapava@ou.edu; Fax: (405) 325-5813

Author

Thao X. D. Nguyen — School of Sustainable Chemical, Biological and Materials Engineering, The University of Oklahoma, Norman, Oklahoma 73019, United States

Complete contact information is available at: https://pubs.acs.org/10.1021/acs.jpcb.3c08092

Notes

The authors declare no competing financial interest.

ACKNOWLEDGMENTS

The authors acknowledge the donors of The American Chemical Society Petroleum Research Fund for partial support of this research through grant PRF # 58518-ND9, and the National Science Foundation (NSF-CBET) for grant CBET 1934513. The use of computing facilities at the University of Oklahoma Supercomputing Center for Education and Research (OSCER) and XSEDE (under allocation CTS-090025) is acknowledged.

REFERENCES

- (1) Bakshi, M. S. Nanoshape control tendency of phospholipids and proteins: protein—nanoparticle composites, seeding, self-aggregation, and their applications in bionanotechnology and nanotoxicology. *J. Phys. Chem. C* **2011**, *115* (29), 13947–13960.
- (2) Kaur, S.; Roy, A. Bioremediation of heavy metals from wastewater using nanomaterials. *Environ., Dev. Sustainability* **2021**, 23, 9617–9640.
- (3) Nguyen, V. T.; Pham, N. H.; Papavassiliou, D. V. Aggregation of nanoparticles and morphology of aggregates in porous media with computations. *J. Colloid Interface Sci.* **2023**, *650* (Pt A), 381–395.
- (4) Shaltiel, L.; Shemesh, A.; Raviv, U.; Barenholz, Y.; Levi-Kalisman, Y. Synthesis and Characterization of Thiolate-Protected Gold Nanoparticles of Controlled Diameter. *J. Phys. Chem. C* **2019**, 123 (46), 28486–28493.
- (5) Kim, M.; Jeon, K.; Kim, W. H.; Lee, J. W.; Hwang, Y.-H.; Lee, H. Biocompatible amphiphilic Janus nanoparticles with enhanced interfacial properties for colloidal surfactants. *J. Colloid Interface Sci.* **2022**, *616*, 488–498.
- (6) Yang, T.; Paulose, T.; Redan, B. W.; Mabon, J. C.; Duncan, T. V. Food and beverage ingredients induce the formation of silver nanoparticles in products stored within nanotechnology-enabled packaging. ACS Appl. Mater. Interfaces 2021, 13 (1), 1398–1412.
- (7) de Lara, L. S.; Rigo, V. A.; Miranda, C. R. Controlling clay swelling-shrinkage with inorganic nanoparticles: a molecular dynamics study. *J. Phys. Chem. C* **2017**, *121* (37), 20266–20271.
- (8) Vu, T. V.; Papavassiliou, D. V. Modification of Oil-Water Interfaces by Surfactant-Stabilized Carbon Nanotubes. *J. Phys. Chem.* C 2018, 122 (48), 27734–27744.
- (9) Lashari, N.; Ganat, T.; Elraies, K. A.; Ayoub, M. A.; Kalam, S.; Chandio, T. A.; Qureshi, S.; Sharma, T. Impact of nanoparticles stability on rheology, interfacial tension, and wettability in chemical

- enhanced oil recovery: A critical parametric review. *J. Pet. Sci. Eng.* **2022**, 212, No. 110199, DOI: 10.1016/j.petrol.2022.110199.
- (10) Miranda, C. R.; de Lara, L. S.; Tonetto, B. C. Stability and Mobility of Functionalized Silica Nanoparticles for Enhanced Oil Recovery Applications, SPE International Oilfield Nanotechnology Conference and Exhibition; OnePetro, 2012.
- (11) Ju, B.; Fan, T.; Ma, M. Enhanced oil recovery by flooding with hydrophilic nanoparticles. *China Particuol.* **2006**, *4* (1), 41–46.
- (12) Lenis, J.; Razavi, S.; Cao, K. D.; Lin, B.; Lee, K. Y. C.; Tu, R. S.; Kretzschmar, I. Mechanical stability of polystyrene and janus particle monolayers at the air/water interface. *J. Am. Chem. Soc.* **2015**, *137* (49), 15370–15373.
- (13) Lan, Y.; Choi, J.; Li, H.; Jia, Y.; Huang, R.; Stebe, K. J.; Lee, D. Janus particles with varying configurations for emulsion stabilization. *Ind. Eng. Chem. Res.* **2019**, *58* (46), 20961–20968.
- (14) Razavi, S.; Lin, B.; Lee, K. Y. C.; Tu, R. S.; Kretzschmar, I. Impact of surface amphiphilicity on the interfacial behavior of Janus particle layers under compression. *Langmuir* **2019**, 35 (48), 15813—15824.
- (15) Correia, E. L.; Brown, N.; Razavi, S. Janus particles at fluid interfaces: Stability and interfacial rheology. *Nanomaterials* **2021**, *11* (2), No. 374, DOI: 10.3390/nano11020374.
- (16) Qiao, Y.; Ma, X.; Liu, Z.; Manno, M. A.; Keim, N. C.; Cheng, X. Tuning the rheology and microstructure of particle-laden fluid interfaces with Janus particles. *J. Colloid Interface Sci.* **2022**, *618*, 241–247.
- (17) Kozina, A.; Ramos, S.; Díaz-Leyva, P.; Castillo, R. Out-of-equilibrium assembly of colloidal particles at air/water interface tuned by their chemical modification. *J. Phys. Chem. C* **2016**, *120* (30), 16879–16886.
- (18) Carrasco-Fadanelli, V.; Castillo, R. Measurement of the capillary interaction force between Janus colloidal particles trapped at a flat air/water interface. *Soft Matter* **2020**, *16* (25), 5910–5914.
- (19) Ruhland, T. M.; Gröschel, A. H.; Ballard, N.; Skelhon, T. S.; Walther, A.; Müller, A. H.; Bon, S. A. Influence of Janus particle shape on their interfacial behavior at liquid—liquid interfaces. *Langmuir* **2013**, 29 (5), 1388—1394.
- (20) Correia, E. L.; Razavi, S. Janus particle amphiphilicity and capillary interactions at a fluid interface. *AIChE J.* **2023**, *69*, No. e18241.
- (21) Chevalier, Y.; Bolzinger, M.-A. Emulsions stabilized with solid nanoparticles: Pickering emulsions. *Colloids Surf., A* **2013**, 439, 23–34.
- (22) Brown, N.; de la Pena, A.; Razavi, S. Interfacial rheology insights: particle texture and Pickering foam stability. *J. Phys.: Condens. Matter* **2023**, 35 (38), No. 384002, DOI: 10.1088/1361-648X/acde2c.
- (23) Binks, B. P.; Fletcher, P. Particles adsorbed at the oil— water interface: A theoretical comparison between spheres of uniform wettability and "Janus" particles. *Langmuir* **2001**, *17* (16), 4708–4710.
- (24) Lei, T.; Luo, K. H. Pore-scale simulation of miscible viscous fingering with dissolution reaction in porous media. *Phys. Fluids* **2021**, 33 (3), No. 034134.
- (25) Prokopev, S.; Vorobev, A.; Lyubimova, T. Phase-field modeling of an immiscible liquid-liquid displacement in a capillary. *Phys. Rev. E* **2019**, 99 (3), No. 033113.
- (26) Soares, E. J.; Thompson, R. L.; Niero, D. C. Immiscible liquid—liquid pressure-driven flow in capillary tubes: Experimental results and numerical comparison. *Phys. Fluids* **2015**, *27* (8), No. 082105.
- (27) Salmo, I. C.; Sorbie, K.; Skauge, A.; Alzaabi, M. Immiscible Viscous Fingering: Modelling Unstable Water—Oil Displacement Experiments in Porous Media. *Transp. Porous Media* **2022**, *145*, 291—322.
- (28) de Castro, A. R.; Oostrom, M.; Shokri, N. Effects of shearthinning fluids on residual oil formation in microfluidic pore networks. *J. Colloid Interface Sci.* **2016**, *472*, 34–43, DOI: 10.1016/j.jcis.2016.03.027.

- (29) Saffman, P. G.; Taylor, G. I. The penetration of a fluid into a porous medium or Hele-Shaw cell containing a more viscous liquid. *Proc. R. Soc. London, Ser. A* **1958**, 245 (1242), 312–329, DOI: 10.1098/rspa.1958.0085.
- (30) Saffman, P. G. Viscous fingering in Hele-Shaw cells. J. Fluid Mech. 1986, 173, 73–94.
- (31) Paterson, L. Radial fingering in a Hele Shaw cell. *J. Fluid Mech.* **1981**, *113*, 513–529.
- (32) Zhang, C.; Oostrom, M.; Wietsma, T. W.; Grate, J. W.; Warner, M. G. Influence of viscous and capillary forces on immiscible fluid displacement: Pore-scale experimental study in a water-wet micromodel demonstrating viscous and capillary fingering. *Energy Fuels* **2011**, 25 (8), 3493–3505.
- (33) Khalilnezhad, A.; Simjoo, M.; Hamidian, N. Insights into viscous fingering effect induced by wettability alteration processes: a fractional flow study. *J. Pet. Sci. Eng.* **2021**, 201, No. 108491.
- (34) Doorwar, S.; Mohanty, K. K. Viscous-fingering function for unstable immiscible flows. SPE J. 2017, 22 (01), 019–031.
- (35) Zhao, B.; Mohanty, K. K. Effect of wettability on immiscible viscous fingering in porous media. *J. Pet. Sci. Eng.* **2019**, *174*, 738–746.
- (36) Tsuzuki, R.; Ban, T.; Fujimura, M.; Nagatsu, Y. Dual role of surfactant-producing reaction in immiscible viscous fingering evolution. *Phys. Fluids* **2019**, *31* (2), No. 022102.
- (37) Ramsden, D.; McKay, K. The degradation of polyacrylamide in aqueous solution induced by chemically generated hydroxyl radicals: Part II—Autoxidation of Fe2+. *Polym. Degrad. Stab.* **1986**, *15* (1), 15–31.
- (38) Ramsden, D.; McKay, K. Degradation of polyacrylamide in aqueous solution induced by chemically generated hydroxyl radicals: Part I—Fenton's reagent. *Polym. Degrad. Stab.* **1986**, *14* (3), 217–229.
- (39) Dong, B.; Yan, Y.; Li, W.; Song, Y. Lattice Boltzmann simulation of viscous fingering phenomenon of immiscible fluids displacement in a channel. *Comput. Fluids* **2010**, 39 (5), 768–779.
- (40) Hoogerbrugge, P. J.; Koelman, J. Simulating microscopic hydrodynamic phenomena with dissipative particle dynamics. *Europhys. Lett. (EPL)* **1992**, *19* (3), No. 155, DOI: 10.1209/0295-5075/19/3/001.
- (41) Groot, R. D.; Warren, P. B. Dissipative particle dynamics: Bridging the gap between atomistic and mesoscopic simulation. *J. Chem. Phys.* **1997**, *107* (11), 4423–4435.
- (42) Pivkin, I. V.; Karniadakis, G. E. A new method to impose noslip boundary conditions in dissipative particle dynamics. *J. Comput. Phys.* **2005**, 207 (1), 114–128.
- (43) Español, P.; Warren, P. Statistical mechanics of dissipative particle dynamics. *Europhys. Lett.* (*EPL*) **1995**, 30 (4), No. 191, DOI: 10.1209/0295-5075/30/4/001.
- (44) Plimpton, S. Fast parallel algorithms for short-range molecular dynamics. *J. Comput. Phys.* **1995**, *117* (1), 1–19.
- (45) Vu, T. V.; Razavi, S.; Papavassiliou, D. V. Effect of Janus particles and non-ionic surfactants on the collapse of the oil-water interface under compression. *J. Colloid Interface Sci.* **2022**, *609*, 158–169.
- (46) Correia, E. L.; Winter, H. H.; Razavi, S. Two-dimensional glass transition—like behavior of Janus particle—laden interface. *Rheol. Acta* **2023**, *62* (4), 239–251.
- (47) Nguyen, T. X. D.; Razavi, S.; Papavassiliou, D. V. Janus Nanoparticle and Surfactant Effects on Oil Drop Migration in Water under Shear. *J. Phys. Chem. B* **2022**, *126* (33), 6314–6323.
- (48) Nguyen, T. X. D.; Vu, T. V.; Razavi, S.; Papavassiliou, D. V. Coarse Grained Modeling of Multiphase Flows with Surfactants. *Polymers* **2022**, *14* (3), No. 543, DOI: 10.3390/polym14030543.
- (49) Humphrey, W.; Dalke, A.; Schulten, K. VMD: visual molecular dynamics. J. Mol. Graphics 1996, 14 (1), 33–38.
- (50) Fernandez-Rodriguez, M. A.; Ramos, J.; Isa, L.; Rodriguez-Valverde, M. A.; Cabrerizo-Vilchez, M. A.; Hidalgo-Alvarez, R. Interfacial activity and contact angle of homogeneous, functionalized,

- and Janus nanoparticles at the water/decane interface. Langmuir 2015, 31 (32), 8818-8823.
- (51) Drelich, A.; Gomez, F.; Clausse, D.; Pezron, I. Evolution of water-in-oil emulsions stabilized with solid particles: Influence of added emulsifier. *Colloids Surf., A* **2010**, 365 (1–3), 171–177.
- (52) Vu, T. V.; Papavassiliou, D. V. Synergistic effects of surfactants and heterogeneous nanoparticles at oil-water interface: Insights from computations. *J. Colloid Interface Sci.* **2019**, *553*, 50–58.
- (53) de Azevedo, M. B.; dos Santos, D.; Faccini, J. L.; Su, J. Experimental study of the falling film of liquid around a Taylor bubble. *Int. I. Multiphase Flow* **2017**, *88*, 133–141.
- (54) Luo, Z. Y.; Shang, X. L.; Bai, B. F. Marangoni effect on the motion of a droplet covered with insoluble surfactant in a square microchannel. *Phys. Fluids* **2018**, *30* (7), No. 077101.
- (55) Tiwari, A.; Abraham, J. Dissipative particle dynamics simulations of liquid nanojet breakup. *Microfluid. Nanofluid.* **2008**, 4, 227–235.
- (56) Zhang, K.; Fang, W.; Ye, S.; Yu, Z.; Chen, S.; Lv, C.; Feng, X.-Q. Drop collision analysis by using many-body dissipative particle dynamics and machine learning. *Appl. Phys. Lett.* **2023**, *123* (20), No. 201601.